

Article

Thermodynamic Assessment of a Solar-Driven Integrated Membrane Reactor for Ethanol Steam Reforming

Hongsheng Wang^{1,2,†}, Bingzheng Wang^{3,†}, Sean-Thomas B. Lundin², Hui Kong^{4,*}, Bosheng Su^{5,6,*} and Jian Wang^{7,*}

¹ MOE Key Laboratory of Hydrodynamic Transients, School of Power and Mechanical Engineering, Wuhan University, Wuhan 430072, China; wanghongsheng@whu.edu.cn

² Department of Chemical System Engineering, School of Engineering, The University of Tokyo, 7-3-1 Hongo, Bunkyo-ku, Tokyo 113-8656, Japan; sean@chemsys.t.u-tokyo.ac.jp

³ Department of Energy Engineering, Zhejiang University, Hangzhou 310027, China; wang_bz@zju.edu.cn

⁴ School of Mechanical Engineering, Beijing Institute of Technology University, Beijing 100081, China

⁵ Department of Marine Equipment and Mechanical Engineering, Jimei University, Xiamen 361021, China

⁶ Fujian Province Key Laboratory of Energy Cleaning Utilization and Development, Xiamen 361021, China

⁷ School of Energy and Environment, City University of Hong Kong, Hong Kong, China

* Correspondence: konghui2020@bit.edu.cn (H.K.); subosheng@jmu.edu.cn (B.S.); jian.wang@cityu.edu.hk (J.W.)

† Equal contribution first authors.

Abstract: To efficiently convert and utilize intermittent solar energy, a novel solar-driven ethanol steam reforming (ESR) system integrated with a membrane reactor is proposed. It has the potential to convert low-grade solar thermal energy into high energy level chemical energy. Driven by chemical potential, hydrogen permeation membranes (HPM) can separate the generated hydrogen and shift the ESR equilibrium forward to increase conversion and thermodynamic efficiency. The thermodynamic and environmental performances are analyzed via numerical simulation under a reaction temperature range of 100–400 °C with permeate pressures of 0.01–0.75 bar. The highest theoretical conversion rate is 98.3% at 100 °C and 0.01 bar, while the highest first-law efficiency, solar-to-fuel efficiency, and exergy efficiency are 82.3%, 45.3%, and 70.4% at 215 °C and 0.20 bar. The standard coal saving rate (SCSR) and carbon dioxide reduction rate (CDRR) are maximums of 101 g·m⁻²·h⁻¹ and 247 g·m⁻²·h⁻¹ at 200 °C and 0.20 bar with a hydrogen generation rate of 22.4 mol·m⁻²·h⁻¹. This study illustrates the feasibility of solar-driven ESR integrated with a membrane reactor and distinguishes a novel approach for distributed hydrogen generation and solar energy utilization and upgradation.

Keywords: solar thermochemistry; ethanol steam reforming (ESR); mid/low-temperature solar energy; hydrogen permeation membrane (HPM); hydrogen generation; thermodynamic efficiency



Citation: Wang, H.; Wang, B.; Lundin, S.-T.B.; Kong, H.; Su, B.; Wang, J. Thermodynamic Assessment of a Solar-Driven Integrated Membrane Reactor for Ethanol Steam Reforming. *Molecules* **2021**, *26*, 6921. <https://doi.org/10.3390/molecules26226921>

Academic Editor: Dongseok Suh

Received: 28 September 2021

Accepted: 15 November 2021

Published: 17 November 2021

Publisher's Note: MDPI stays neutral with regard to jurisdictional claims in published maps and institutional affiliations.



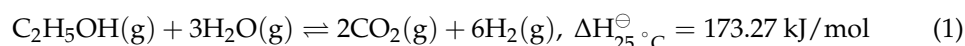
Copyright: © 2021 by the authors. Licensee MDPI, Basel, Switzerland. This article is an open access article distributed under the terms and conditions of the Creative Commons Attribution (CC BY) license (<https://creativecommons.org/licenses/by/4.0/>).

1. Introduction

The combustion of fossil fuels worldwide is releasing an enormous quantity of CO₂ into the atmosphere that is considered largely responsible for environmental problems (e.g., global warming, NO_x and SO_x pollution). Solar energy is a clean and abundant form of energy with the potential to solve these long-term energy and environmental issues [1]. However, due to the intermittency and low energy density of solar irradiation, solar energy must be converted into stable chemical fuels to create a steady solar energy supply [2]. Hydrogen is considered a green energy carrier, which balances energy density with the capabilities of both long-term storage and ease of conversion to other energy forms [3,4]. Hydrogen can be produced by several solar thermochemical reactions [5–7], wherein the fuel reforming process driven by solar energy can generate hydrogen efficiently [8,9].

Among the various fuels, biofuels such as bioethanol are considered to be carbon neutral because the CO₂ emitted upon combustion was originally absorbed during the growth of the plants [10]. Bioethanol can be produced from secondary biomass, and it has

been estimated that more than 442 billion liters of bioethanol can be yielded each year if all the agricultural residues, forestry wastes, and dedicated energy crops are utilized [11,12]. More than 110 billion liters of bioethanol are produced worldwide each year, and the USA and Brazil are the two major producers, producing around 85% of the global bioethanol production [13,14]. Converting bioethanol into hydrogen via solar thermochemical process allows for the simultaneous production of green hydrogen and storage of solar energy. The primary pathway for this is ethanol steam reforming (ESR, shown in Equation (1)) [15]:



One drawback of hydrogen is the complexity and associated cost of transportation over liquid fuels. Thus, on-site hydrogen generation from ESR offers an economic pathway for distributed energy systems, such as refueling stations for hydrogen fuel cell powered vehicles. The H_2 and CO_2 products of ESR need to be separated for hydrogen utilization and carbon capture. However, industrial gas separation technologies such as pressure swing adsorption are not sufficiently cost-efficient for small-scale distributed hydrogen refueling stations [16]. Coupling ESR with hydrogen permeation membranes (HPM) in a membrane reactor configuration allows for the selective removal of hydrogen driven by its partial pressure difference between the catalyst bed and the permeate side of the membrane. In addition to single-step ethanol conversion and hydrogen separation, the membrane reactor causes a forward equilibrium shift, which reduces the required reaction temperature and increase the conversion rate. HPMs are made from various materials, including ceramic, polymeric, perovskite, and metallic membranes [17]. Among them, dense metallic membranes offer high selectively and H_2 permeance. In particular, Pd-Ag membranes are studied because of the ability to inhibit hydrogen embrittlement at lower temperatures [18–20]. Pd-Ag membranes are commonly fabricated on porous ceramic supports, which allows them to withstand a high-pressure difference between the two sides of the membrane [21]. Iulianelli et al. had experimentally proved in different research studies that the bioethanol steam reforming in a Pd-based HPM reactor can obtain a higher bioethanol conversion rate than that in a traditional reactor with the catalysts of Co–Pt [22] and Ni/CeO₂ [23].

The large enthalpy change of ESR and pre-heating of reactants requires a large thermal energy input, which is traditionally provided by fossil fuel combustion leading to additional CO₂ emissions [19]. With the rapid development of concentrated solar energy (CSE) technologies, solar thermochemical reactions have become an alternative that decreases the consumption of fossil fuels [24–27]. In most solar thermochemical reactions, solar collectors are used to collect and convert solar energy into thermal energy. Point-focusing solar collectors, such as dish collectors and heliostat field collectors, concentrate sunlight into a point and induce high temperatures in the materials (e.g., 2000 °C) [28]. In contrast, line-focusing parabolic trough solar collectors allow temperatures to be maintained below 500 °C, making them one of the most economical methods of utilizing solar energy [29]. Nevertheless, both types of collectors have attracted increasing attention in recent years. Bai et al. experimentally realized an industrial-scale mid-temperature thermochemical power generation using a structure combining a solar thermal collector and a reactor for methane synthesis [30]. Wang et al. [31] modeled a solar dish collector integrated with HPM for non-oxidative methane dehydroaromatization in the temperature range of 600 °C to 800 °C and obtained a theoretical energy efficiency of 85.9%. Tou et al. [32] experimentally demonstrated the single-step continuous splitting of CO₂ into separate streams of CO and O₂ under steady-state isothermal/isobaric conditions using a solar-driven ceria membrane reactor. Operation at 1600 °C, 3×10^{-6} bar P_{O_2} , and 3500 sun radiation resulted in an O₂ separation rate of 0.024 $\mu\text{mol}\cdot\text{s}^{-1}\cdot\text{cm}^{-2}$. Giaconia [33] studied methane steam reforming using a membrane reactor driven by concentrated solar power and achieved a conversion rate twice that of a conventional reformer operating at thermodynamic equilibrium. He et al. [5] modeled propane dehydrogenation using a trough solar collector combined with a membrane reactor and observed a maximum propane conversion rate and propylene yield

of 99.2% and 98.3% at a reaction temperature of 400 °C and permeate pressure of 10^{-5} bar. In each study, the presence of the membrane reactor enhances efficiencies as compared with the use of traditional reactors without membrane.

Although the kinetics and catalytic processes of ESR have been widely studied [34], the thermodynamic and environmental performance of a solar-driven ESR membrane reactor have not been researched. Thus, a novel solar-driven ESR system combined with an HPM reactor is proposed and analyzed. This system allows for the conversion of intermittent low-grade solar thermal energy into high-grade chemical energy. The thermodynamic efficiencies and conversion rates are optimized and compared with those using a traditional reactor. The carbon dioxide emissions reduction rate (CDRR) and standard coal savings rate (SCSR) were also calculated to gauge the environmental performance of this system.

2. System Description

A conceptual schematic of a solar-driven ESR membrane reactor is shown in Figure 1a. Heat energy is collected from solar irradiation by a trough solar collector, which subsequently is either used directly to drive the ESR membrane reactor or stored for later use in a hot tank. The ESR membrane reactor consists of a packed-bed tube-in-shell configuration. The exterior shell is impermeable, while the interior tube is an HPM consisting of a supported Pd-Ag composite membrane. The packed-bed (feed side) consists of a commercial nickel-based catalyst [35] to catalyze the ESR reaction, while the permeate side is connected to a vacuum pump that maintains a pressure conducive for hydrogen separation.

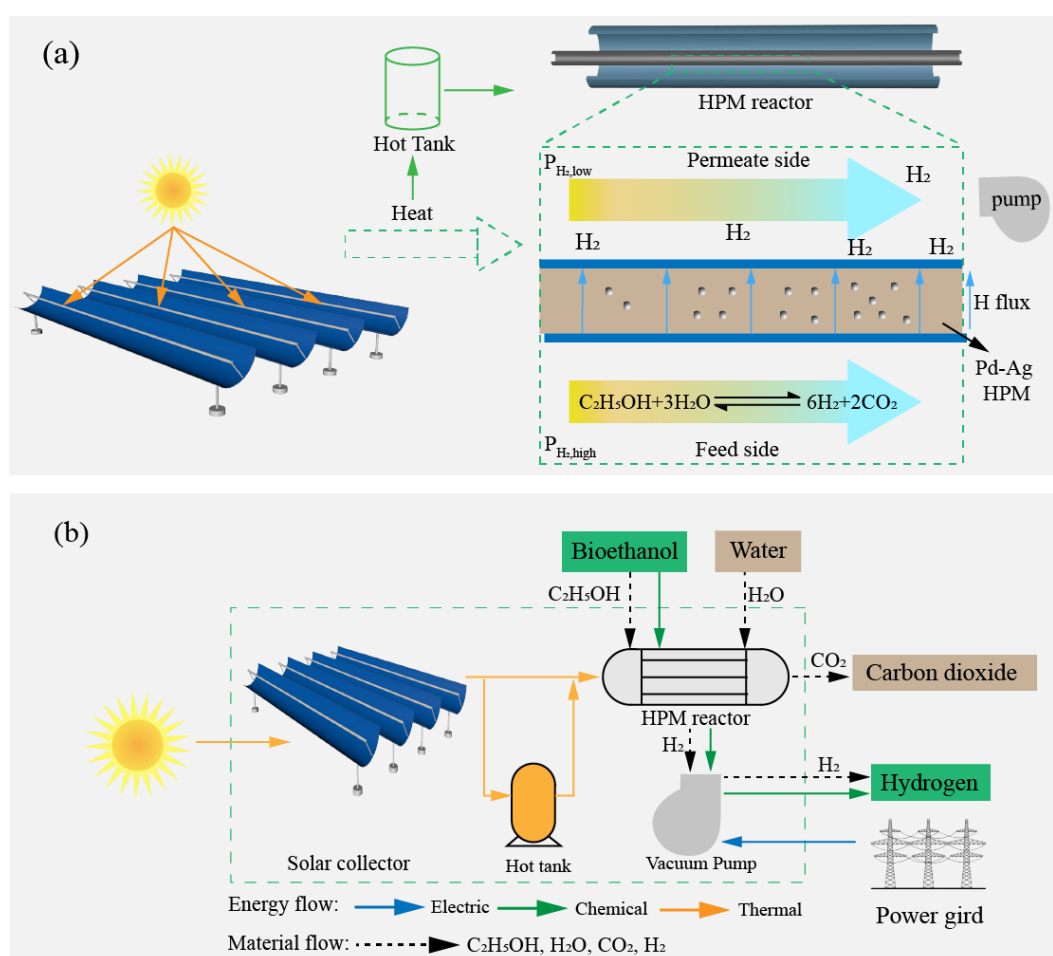


Figure 1. Conceptual schematic (a) and system boundary containing input/output flows (b) of a solar-driven ESR membrane reactor.

Figure 1b shows the main input/output flows of the system. The input water and ethanol are preheated to the reaction temperature by solar thermal energy before being fed at the stoichiometric molar ratio of $H_2O:C_2H_5OH = 3:1$, and the high purity hydrogen and carbon dioxide are the system material output. Solar energy, chemical energy of ethanol, and electric energy are the input energy of the system, and chemical energy of hydrogen is the system output energy. In the reaction process, generated hydrogen permeates through the HPM driven by the pressure difference between the feed and permeate sides, which increases the conversion rate of ESR and purifies the hydrogen. The main simulation work is completed by Python 3.6.6, and the required thermodynamic parameters are provided by HSC software. The thermodynamic results are obtained based on the following assumptions:

- (1) Steady-state operation of the ESR membrane reactor is assumed [36];
- (2) Pressure-drop across the catalyst bed is negligible [37];
- (3) Ideal plug-flow operation is assumed (i.e., gas diffusion is negligible) [38].

3. Theoretical Formulations

Thermodynamic efficiencies offer insight into the capability of a system to convert and utilize solar energy and are thus systematically analyzed. Herein, the first-law thermodynamic efficiency, solar-to-fuel efficiency, and exergy efficiency are chosen as three key indicators for gauging the thermodynamic performance of the system. The first-law thermodynamic efficiency (η_{HHV} , Equation (2)) is the ratio of system energy output to energy input, and is expressed as [39]

$$\eta_{HHV} = \frac{n_{H_2} \cdot HHV_{H_2}}{\eta_{opt}^{-1} \eta_{abs}^{-1} \cdot (Q_{preheat} + Q_{enthalpy}) + \eta_{s \rightarrow e}^{-1} \cdot W_p + n_E \cdot HHV_E} \quad (2)$$

where n_{H_2} and n_E are the molar amount of generated hydrogen and consumed ethanol; HHV_{H_2} and HHV_E are the molar higher heating value of hydrogen and ethanol, taken as $286 \text{ kJ} \cdot \text{mol}^{-1}$ and $1410 \text{ kJ} \cdot \text{mol}^{-1}$ [40]; η_{opt} is the optical efficiency of the trough solar collector, taken as 73% [41]; η_{abs} exhibited by Equation (3) is the absorption efficiency of the collector, expressed as [42]

$$\eta_{abs} = \alpha - \frac{\varepsilon \cdot \sigma \cdot (T_H + 273.15)^4}{DNI \cdot C_{collector}} \quad (3)$$

where α and ε are the absorptivity and emissivity of the collector, taken as 0.9 and 0.1 [42]; σ is Stefan–Boltzmann's constant; T_H is the reaction temperature; DNI is the direct normal irradiation; $C_{collector}$ is the concentration ratio of the collector; $\eta_{s \rightarrow e}$ is the solar-to-electric efficiency, taken as 15% (commercial photovoltaic (PV) cell efficiency) and 40% (multiple-junction GaAs PV efficiency in laboratory). $Q_{preheat}$ is the heat consumed to raise the temperatures of ethanol and water from room temperature to reaction temperature and is calculated as Equation (4) [31,40]:

$$Q_{preheat} = n_{E,init} \cdot \left(\int_{T_L}^{78} C_{p,C_2H_5OH(l)} dT + 39.234 + n_{E,init} \cdot \int_{78}^{T_H} C_{p,C_2H_5OH(g)} dT \right) + n_{W,init} \cdot \left(\int_{T_L}^{100} C_{p,H_2O(l)} dT + 40.873 + \int_{100}^{T_H} C_{p,H_2O(g)} dT \right) \quad (4)$$

where $n_{E,init}$ and $n_{H_2O,init}$ are the initial molar amounts of ethanol and water; $C_{p,E}$ and C_{p,H_2O} are the specific heat capacities of ethanol and water; 39.234 and 40.873 ($\text{kJ} \cdot \text{mol}^{-1}$) are the molar vaporization latent heat of ethanol and water [40]. $Q_{enthalpy}$ is the heat consumed by the enthalpy change of ESR reaction; W_p is the exergy consumed by the vacuum pump to maintain a low pressure for hydrogen separation, and expressed as Equation (5):

$$W_p = n_{H_2,out} \cdot RT_0 \ln(P_0/P_{H_2,out}) \quad (5)$$

where $n_{\text{H}_2,\text{out}}$ is the molar amount of separated hydrogen; R is universal gas constant, taken as $8.314 \text{ J}\cdot\text{mol}^{-1}\cdot\text{K}^{-1}$; T_0 is the room temperature, given as 25°C ; P_0 is the reaction pressure, fixed at 1 bar in this research; $P_{\text{H}_2,\text{out}}$ is the permeate pressure. In thermodynamic equilibrium state, the hydrogen partial pressure should be equal on two sides of the HPM, and thus the $n_{\text{H}_2,\text{out}}$ can be derived as Equation (6):

$$n_{\text{H}_2,\text{out}} = \frac{2 \cdot n_{\text{E,init}} \cdot (3 \cdot \alpha_0 \cdot P_0 - 2 \cdot \alpha_0 \cdot P_{\text{H}_2,\text{out}} - 2 \cdot P_{\text{H}_2,\text{out}})}{P_0 - P_{\text{H}_2,\text{out}}} \quad (6)$$

where α_0 is the conversion rate of ESR.

The η_{HHV} can exhibit the total energy conversion and utilization capability of this system. While the energy input in η_{HHV} calculation contains the chemical energy of ethanol, to eliminate the influence of chemical energy in reactants and evaluate the conversion from solar energy to chemical energy in products, the solar-to-fuel efficiency ($\eta_{\text{s}\rightarrow\text{f}}$), which is defined as the ratio of chemical energy increment to solar energy input, is expressed as Equation (7):

$$\eta_{\text{s}\rightarrow\text{f}} = \frac{n_{\text{H}_2} \cdot \text{HHV}_{\text{H}_2} - n_{\text{E}} \cdot \text{HHV}_{\text{E}}}{\eta_{\text{opt}}^{-1} \eta_{\text{abs}}^{-1} \cdot (Q_{\text{preheat}} + Q_{\text{enthalpy}}) + \eta_{\text{s}\rightarrow\text{e}}^{-1} \cdot W_{\text{p}}} \quad (7)$$

In Equations (2) and (7), W_{p} , the consumed vacuum pump exergy (theoretical minimum energy), is used to calculate the upper bound of thermodynamic efficiencies and exhibits the potential of this system in further application. The vacuum pump efficiency is the ratio of exergy output to electricity input of the vacuum pump, calculated as Equation (8) [43,44]:

$$\eta_{\text{p}} = \left(\frac{P_{\text{H}_2,\text{out}}}{P^\ominus} \right)^{0.544} \quad (8)$$

where P^\ominus is the standard pressure. After taking the vacuum pump efficiency into consideration, the first-law efficiency and solar-to-fuel efficiency with real separation energy ($\eta_{\text{HHV,real}}$ and $\eta_{\text{s}\rightarrow\text{f,real}}$) can be expressed as Equations (9) and (10):

$$\eta_{\text{HHV,real}} = \frac{n_{\text{H}_2} \cdot \text{HHV}_{\text{H}_2}}{\eta_{\text{opt}}^{-1} \eta_{\text{abs}}^{-1} \cdot (Q_{\text{preheat}} + Q_{\text{enthalpy}}) + \eta_{\text{s}\rightarrow\text{e}}^{-1} \eta_{\text{p}}^{-1} \cdot W_{\text{p}} + n_{\text{E}} \cdot \text{HHV}_{\text{E}}} \quad (9)$$

$$\eta_{\text{s}\rightarrow\text{f,real}} = \frac{n_{\text{H}_2} \cdot \text{HHV}_{\text{H}_2} - n_{\text{E}} \cdot \text{HHV}_{\text{E}}}{\eta_{\text{opt}}^{-1} \eta_{\text{abs}}^{-1} \cdot (Q_{\text{preheat}} + Q_{\text{enthalpy}}) + \eta_{\text{s}\rightarrow\text{e}}^{-1} \eta_{\text{p}}^{-1} \cdot W_{\text{p}}} \quad (10)$$

Equations (2), (7), (9) and (10) mainly focus on the energy conversion amount, while the conversion efficiency of energy quality is also significant. The exergy efficiency (η_{ex}), which is the ratio of exergy output to exergy input, is defined as Equation (11) [39,45]:

$$\eta_{\text{ex}} = \frac{n_{\text{H}_2} \cdot \text{Ex}_{\text{H}_2}}{\text{Ex}_{\text{solar}} + n_{\text{E}} \cdot \text{Ex}_{\text{E}}} \quad (11)$$

$$\text{Ex}_{\text{solar}} = \left(1 - \frac{4T_0}{3T_{\text{sun}}} + \frac{1}{3} \cdot \left(\frac{T_0}{T_{\text{sun}}} \right)^4 \right) \cdot \left((Q_{\text{preheat}} + Q_{\text{enthalpy}}) \cdot \eta_{\text{opt}}^{-1} \eta_{\text{abs}}^{-1} + \eta_{\text{s}\rightarrow\text{e}}^{-1} \eta_{\text{p}}^{-1} \cdot W_{\text{p}} \right) \quad (12)$$

where Ex_{H_2} and Ex_{E} are the chemical exergies of hydrogen and ethanol, taken as $235 \text{ kJ}\cdot\text{mol}^{-1}$ and $1308 \text{ kJ}\cdot\text{mol}^{-1}$; Ex_{solar} calculated by Equation (12) is the input exergy of solar energy.

In addition to the thermodynamic performance, the environmental performance is also considered in terms of the fossil fuel saved (SCSR, Equation (13)) and CO_2 emissions reduced (CDRR, Equation (14)). Assuming the absorbed solar energy is provided by standard coal, the SCSR and CDRR can be defined as

$$\text{SCSR} = \frac{\eta_{\text{c}\rightarrow\text{h}}^{-1} \cdot (\dot{Q}_{\text{preheat}} + \dot{Q}_{\text{enthalpy}}) + \eta_{\text{c}\rightarrow\text{e}}^{-1} \cdot \eta_{\text{p}}^{-1} \cdot \dot{W}_{\text{p}}}{q_{\text{coal}}} \quad (13)$$

$$\text{CDRR} = \mu \cdot \text{SCSR} \quad (14)$$

where $\eta_{c \rightarrow h}$ and $\eta_{c \rightarrow e}$ are conversion efficiencies from standard coal to heat and electricity, which are taken as 80% and 40% [46,47]; q_{coal} is the heating value of standard coal, taken as $2.931 \times 10^4 \text{ kJ} \cdot \text{kg}^{-1}$; and μ is the mass ratio of carbon dioxide emissions to standard coal combustion, taken as 2.45 [48].

4. Results and Discussion

The proposed system was investigated and analyzed by numerical simulation and calculation. With a feed pressure of 1 bar, the thermodynamic and environmental performances were studied for temperatures of 100 °C to 400 °C and permeate pressures of 0.01 bar to 0.75 bar. To verify the simulated reaction results, the conversion rate of ethanol in this research is compared with the experimental results [49], which are under the temperature range of 250–320 °C and reaction pressure of 1 bar without hydrogen separation, shown in Figure 2. The experimental conversions are slightly higher than the thermodynamic results in this simulation due to the potential side reactions (e.g., ethanol splitting), while the deviation is smaller than 5%, which denotes that the simulation results fit well with those from the experiment.

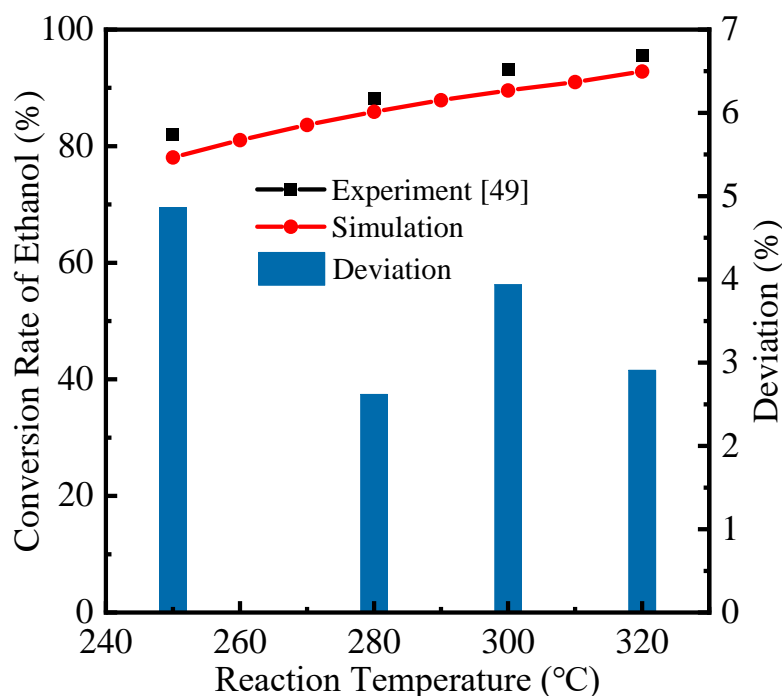


Figure 2. Comparison between theoretical and experimental ethanol conversion rate of ESR for model validation.

Figure 3 exhibits the conversion rate of ESR under different reaction temperatures and permeate pressures. The endothermicity of ESR means that the thermodynamic equilibrium conversion will increase with increasing temperature. Decreasing permeate pressure increases the removal of the generated hydrogen by the HPM reactor, which then increases the conversion rate of ESR due to Le Chatelier's principle. However, the grey zone in Figure 3 represents the region wherein the permeate pressure is higher than the hydrogen partial pressure in equilibrium, meaning that the HPM has no driving force and cannot remove the generated hydrogen. The upper bound of the colored area denotes the equilibrium-limited conversion rate without hydrogen separation. At 100 °C, the equilibrium conversion rate of a traditional reactor is 14.8%, and the corresponding hydrogen partial pressure is 0.19 bar. By lowering the permeate pressure to 0.01 bar, the generated hydrogen can be removed, causing the conversion rate to increase to 98.3%. At

300 °C, however, the traditional reactor already results in an equilibrium conversion of 89.6%, so the presence of the HPM and low permeate pressure has a lower effect. Operating at higher temperatures consumes more thermal energy and separation work with less increase in conversion, which negatively influences the thermodynamic efficiencies of the system.

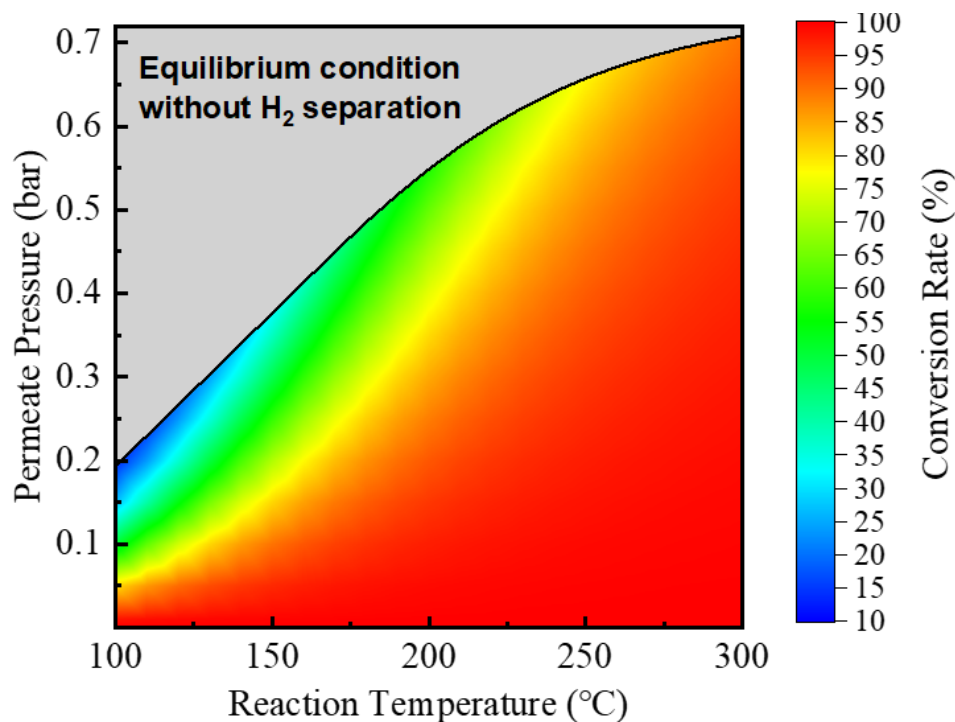


Figure 3. ESR conversion rate at different reaction temperatures and permeate pressures.

Figure 4 shows various thermodynamic efficiencies (Equations (2), (7), (9), (10) and (11)) under different permeate pressures at a temperature of 150 °C. The line type distinguishes different solar-to-electric efficiencies ($\eta_{s \rightarrow e}$ of 15% or 40%). The upper bound efficiencies are given when separation exergy is used (η_{HHV} and $\eta_{s \rightarrow f}$), whereas the best efficiencies using common separation methods such as vacuum pumping are calculated using real separation energy ($\eta_{HHV,real}$ and $\eta_{s \rightarrow f,real}$). The difference between these values is the potential for improvement in efficiency if the separation method is improved.

Permeate pressure affects the pump efficiency (η_p), hydrogen separation exergy (W_p), and conversion rate, which leads to an optimum efficiency at some specific permeate pressure for each calculation. This is the result of two different competing influences. As shown in Figure 3, increasing the permeate pressure decreases the conversion rate, which results in lower solar energy conversion into chemical energy and a corresponding negative influence on efficiencies. Simultaneously, the pump efficiency is increased at higher permeate pressures, which reduces the required separation exergy and corresponding separation energy of the vacuum pump. Optimization of efficiencies using separation exergy and $\eta_{s \rightarrow e} = 40\%$ results in maximums for η_{HHV} , $\eta_{s \rightarrow f}$, and η_{ex} of 81.8%, 44.4%, and 64.2% at a permeate pressure of 0.08 bar; optimization of efficiencies using real separation energy results in maximums for $\eta_{HHV,real}$ and $\eta_{s \rightarrow f,real}$ of 77.1% and 37.4% at a permeate pressure of 0.18 bar.

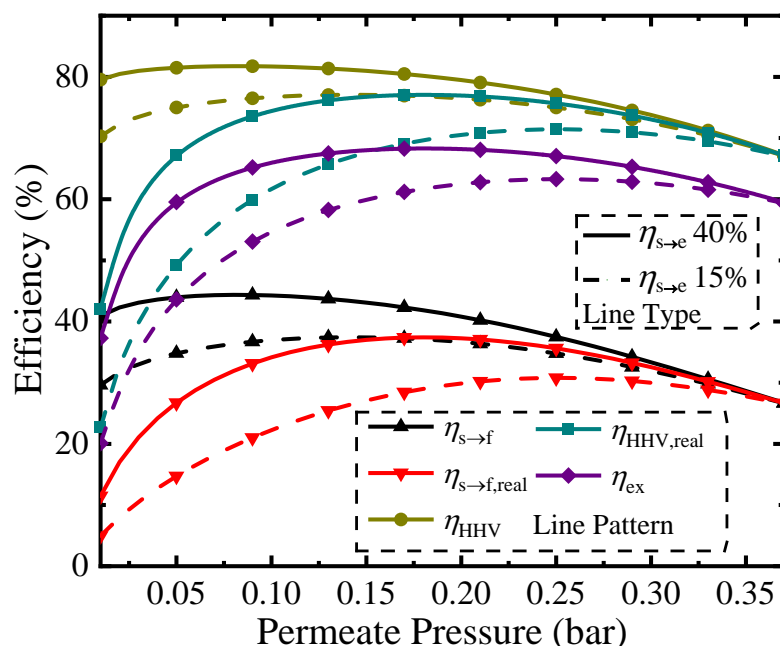


Figure 4. Thermodynamic efficiency versus permeate pressure at a reaction temperature of 150 °C.

In addition to the permeate pressure, reaction temperature has a significant effect on performance. Because Figure 3 shows that a permeate pressure of 0.2 bar can separate hydrogen at nearly all temperatures, the permeate pressure was set to 0.2 bar, and the thermodynamic efficiencies were calculated for temperatures of 100 °C to 400 °C (Figure 5). The reaction temperature affects the preheating energy, enthalpy change, and conversion rate. As the temperature increases, all efficiencies initially increase and then decrease. This efficiency maximum occurs because the increase in conversion with increasing temperature is balanced by an increase in energy consumption to preheat the reactants. With the $\eta_{s \rightarrow e}$ of 40%, these effects balance at a temperature of 215 °C using separation exergy, resulting in maximum thermodynamic efficiencies for η_{HHV} , $\eta_{s \rightarrow f}$, and η_{ex} with separation exergy of 82.3%, 45.3%, and 70.4%. The corresponding maximum using separation energy occurs at 210 °C, resulting in $\eta_{HHV,real}$ and $\eta_{s \rightarrow f,real}$ of 79.4% and 40.7%.

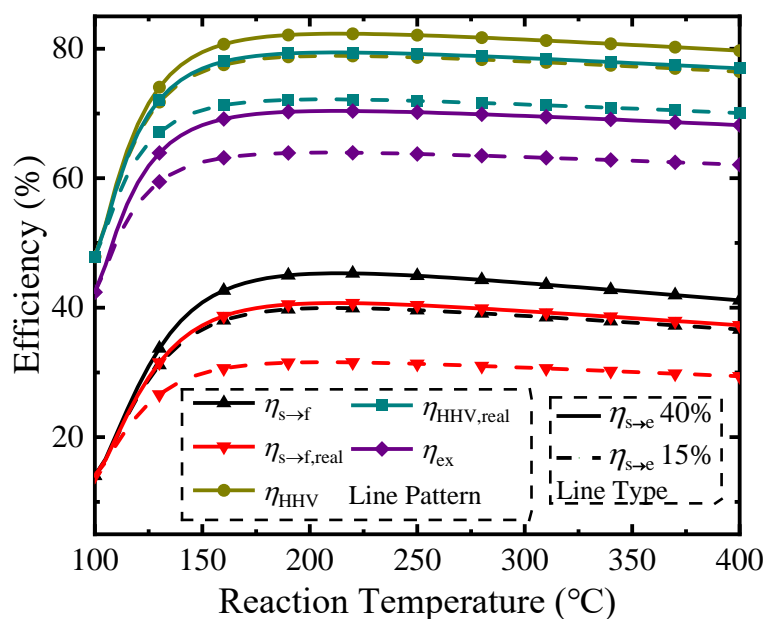


Figure 5. Thermodynamic efficiency versus temperature for a permeate pressure of 0.2 bar.

While the analyses of Figures 3 and 4 are useful for a qualitative determination of system efficiencies, an analysis concerning the change in efficiency versus kJ of hydrogen energy formed is necessary for a quantitative assessment of the proposed system. Figure 6 exhibits the energy consumption variation per kJ of hydrogen energy generated using real separation energy and $\eta_{s \rightarrow e}$ of 15%. The energy consumption consists of the enthalpy change, preheating, vacuum pump, and chemical energy of reactants. The chemical energy consumption is assumed to be constant due to the fixed stoichiometric ratio in this research.

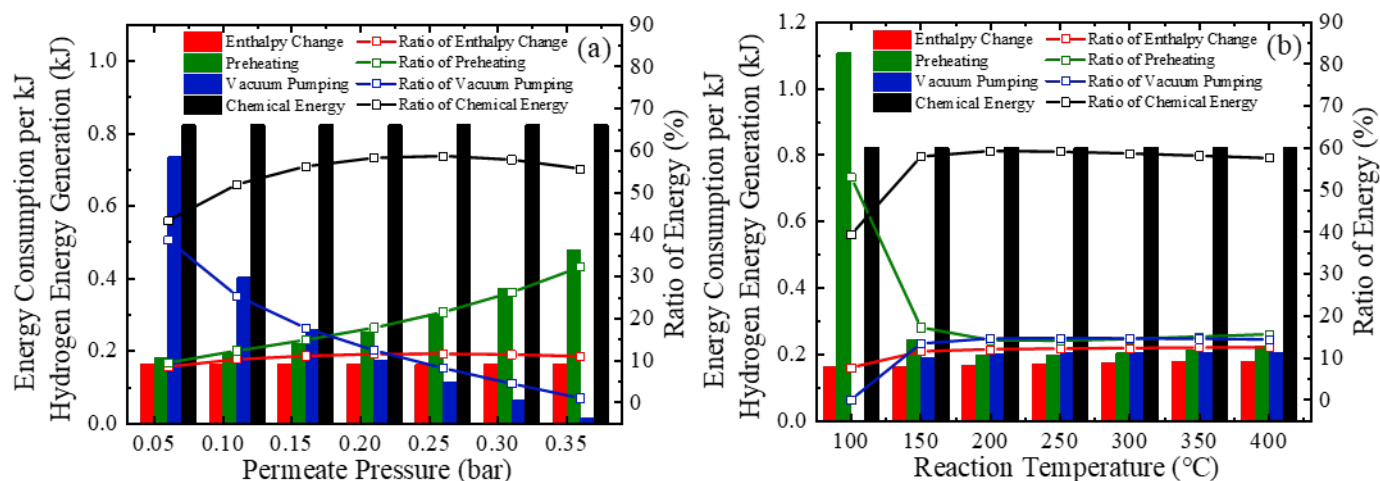


Figure 6. Energy consumption per kJ hydrogen energy generated ($\eta_{s \rightarrow e} = 15\%$) under (a) different permeate pressures (reaction temperature of 150 °C) and (b) different reaction temperatures (permeate pressure of 0.2 bar).

In Figure 6a the preheating energy increases with increasing permeate pressure because increasing permeate pressure reduces conversion and results in a larger feed rate to be preheated per kJ hydrogen energy. Simultaneously, the energy consumed by the vacuum pump decreases due to a decrease in the separation exergy (W_p) and increase in pump efficiency (η_p). This results in an optimal permeate pressure of c.a. 0.25 bar.

The energy consumption dependence with reaction temperature is shown in Figure 6b. The enthalpy change of Equation (1) has a slight increase from 100 °C to 400 °C ($179 \text{ kJ} \cdot \text{mol}^{-1}$ to $197 \text{ kJ} \cdot \text{mol}^{-1}$), and thus the energy consumed of enthalpy change goes up. At any permeate pressure, the pump efficiency is constant and the quantity of hydrogen separated per kJ hydrogen energy generated can be expressed as Equation (6) divided by the amount of hydrogen generated, shown in Equation (15) as follow:

$$n_{\text{H}_2, \text{out, per}} = \frac{\left(3 \cdot P_0 - 2 \cdot P_{\text{H}_2, \text{out}} - \frac{2 \cdot P_{\text{H}_2, \text{out}}}{\alpha_0}\right)}{3 \cdot (P_0 - P_{\text{H}_2, \text{out}})} \quad (15)$$

This indicates that the conversion rate (α_0) increases along with rising temperature, meaning the pump work increase slightly due to the increase in separated hydrogen, as shown in Figure 6b. Note that at 100 °C the hydrogen partial pressure in equilibrium is slightly less than 0.2 bar (Figure 3), so the consumed vacuum pump energy is zero. The energy required for preheating shows a maximum at c.a. 200 °C because of opposing influences arising from conversion rate and reaction temperature.

The thermodynamic efficiency under different temperatures and permeate pressures is shown in Figure 7. In the ESR membrane reactor, the hydrogen is generated and purified in a single step, which increases conversion and eliminates the requirement for a separate separation process downstream. At higher temperatures (e.g., greater than 280 °C in Figure 7a–e), the optimal efficiencies are obtained in the absence of hydrogen separation. This is because the use of a vacuum pump leads to additional energy consumption, while the conversion rate cannot be significantly improved due to the already high thermodynamic limitation of ESR at high temperatures. The highest η_{HHV} , $\eta_{s \rightarrow f}$, and η_{ex}

can be 82.17%, 45.06%, and 72.83% at 320 °C without hydrogen separation. Instead, the solar-driven ESR membrane reactor is beneficial at lower temperatures due to increased efficiencies, which results in lower requirements for irradiation intensity and longer working hours. In the case of higher irradiation intensity, the reactant flow rate can be increased to obtain a higher yield.

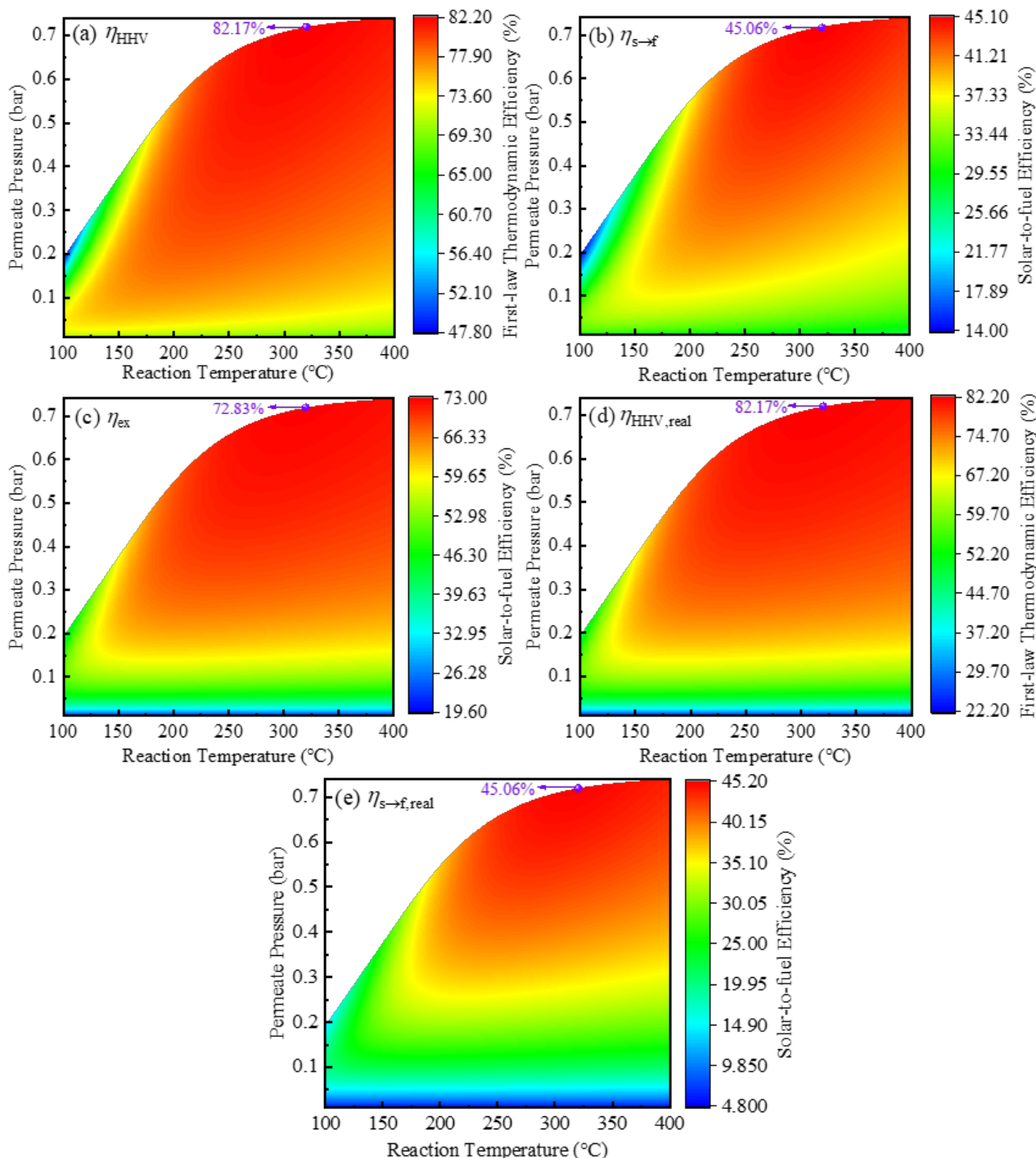


Figure 7. Thermodynamic efficiencies containing (a) η_{en} , (b) $\eta_{s \rightarrow f}$, (c) η_{ex} , (d) $\eta_{en,real}$, and (e) $\eta_{s \rightarrow f,real}$ versus temperature and permeate pressure. The maximum efficiency has been marked in the subfigures as purple points.

To clearly illustrate the benefits of the proposed ESR membrane reactor over a traditional reactor without hydrogen separation, a plot of the efficiency improvement increments versus permeate pressure at 150 °C is shown in Figure 8. At 150 °C, the equilibrium

pressure of hydrogen is 0.37 bar, so the membrane reactor only improves the system for permeate pressures below this level. The conversion increases with decreasing permeate pressure due to the increasing driving force for hydrogen separation, with a maximum increase of 66.3% achieved at a permeate pressure of 0.01 bar. However, according to Equations (5) and (8), the increase in exergy and decrease in pump efficiency causes a maximum in the thermodynamic efficiencies to appear. Regarding the separation exergy, the improvement over a traditional reactor for η_{HHV} , $\eta_{s \rightarrow f}$, and η_{ex} can achieve 15.1%, 18.1%, and 5.21% at 0.08 bar with $\eta_{s \rightarrow e} = 40\%$, respectively. As for the efficiencies regarding real separation energy, the $\eta_{HHV,real}$ and $\eta_{s \rightarrow f,real}$ can achieve maximum increases of 10.4% and 11.2% at 0.18 bar and $\eta_{s \rightarrow e}$ of 40%.

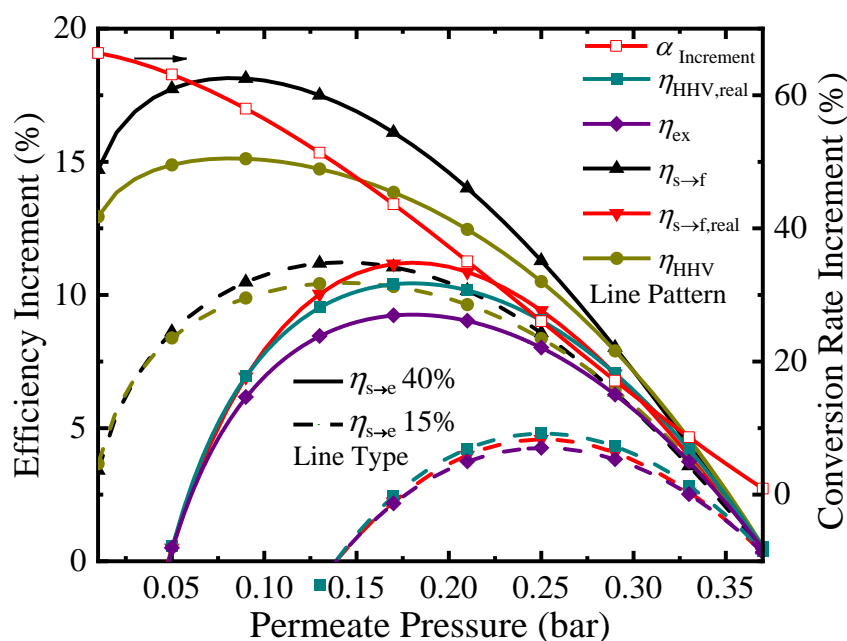


Figure 8. Increment of thermodynamic efficiency and conversion rate compared with those in a traditional reactor versus permeate pressure at a reaction temperature of 150 °C.

Figure 9 exhibits the increment of thermodynamic efficiency and conversion rate compared with those in a traditional reactor under different reaction temperatures at a permeate pressure of 0.2 bar. At 100 °C, the hydrogen partial pressure at equilibrium condition in a traditional reactor is 0.19 bar, so the membrane reactor with a permeate pressure of 0.2 bar cannot improve the operation. However, as the temperature increases, the hydrogen partial pressure increases. An increased hydrogen partial pressure allows for a faster removal of hydrogen using a membrane, which causes an increase in the conversion. The largest conversion increase is 40.3% at 170 °C, whereupon further temperature increases observe a decrease in conversion improvement due to the limited improvement potential from an already high thermodynamic limitation of ESR, coupled with an increase in energy consumption of preheating and enthalpy change. With $\eta_{s \rightarrow e} = 40\%$, the $\eta_{s \rightarrow f,real}$ has a maximum increment of 11.3% at 140 °C, and the $\eta_{HHV,real}$ has a maximum increment of 12.0% at 130 °C.

In addition to the thermodynamic performance, environmental performance is also vital for the evaluation of this system. Variation of SCSR, CDRR, and hydrogen generation rate (Y_{H_2}) with real separation energy and $\eta_{s \rightarrow e}$ of 15% under different working conditions are shown in Figure 10. Solar energy is collected and stored in a hot tank to supply heat to the ESR membrane reactor. The DNI determines the amount of available energy. Figure 10a exhibits the SCSR, CDRR, and Y_{H_2} with real separation energy under different permeate pressures at 150 °C. The amount of input energy at a certain DNI is constant, and thus a higher $\eta_{s \rightarrow f,real}$ shown in Figure 4 can reach a higher Y_{H_2} . The highest Y_{H_2} is

$36.3 \text{ mol}\cdot\text{m}^{-2}\cdot\text{h}^{-1}$ at 0.25 bar, DNI of $1000 \text{ W}\cdot\text{m}^{-2}$. In the calculation of SCSR, the $\eta_{c\rightarrow e}$ and $\eta_{s\rightarrow e}$ are taken as 40% and 15%, and thus when energy is used to generate electricity, 1 kJ solar energy can be considered as equal to 0.375 kJ (15%/40%) chemical energy of standard coal. The $\eta_{c\rightarrow h}$ is 80%, and the conversion efficiency of solar to heat can be considered as the product of optical efficiency and absorption efficiency, which is about 65.7% in this research, and thus 1 kJ solar energy is equivalent to 0.821 kJ (65.7%/80%) chemical energy of standard coal when the energy is used to generate heat. Thus, increasing the proportion of solar energy consumed in the form of thermal energy results in increases in SCSR and CDRR based on Equation (13). The highest Y_{H_2} at DNI of $1000 \text{ W}\cdot\text{m}^{-2}$ results in an SCSR and CDRR of $88.7 \text{ g}\cdot\text{m}^{-2}\cdot\text{h}^{-1}$ and $217 \text{ g}\cdot\text{m}^{-2}\cdot\text{h}^{-1}$. In Figure 10b, the trends of SCSR, CDRR, and Y_{H_2} are the same as those in Figure 10a. The highest Y_{H_2} at a DNI of $1000 \text{ W}\cdot\text{m}^{-2}$ ($22.4 \text{ mol}\cdot\text{m}^{-2}\cdot\text{h}^{-1}$) is obtained at 200°C , with a corresponding SCSR and CDRR of $101 \text{ g}\cdot\text{m}^{-2}\cdot\text{h}^{-1}$ and $247 \text{ g}\cdot\text{m}^{-2}\cdot\text{h}^{-1}$.

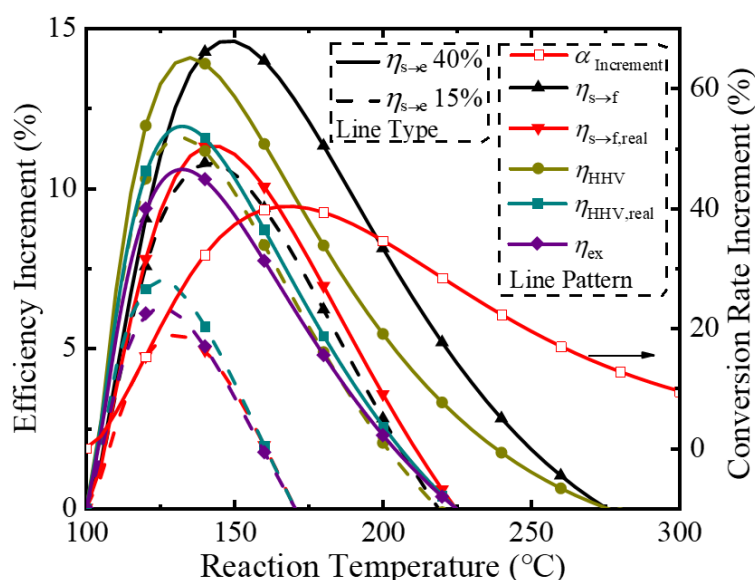


Figure 9. Increment of thermodynamic efficiency and conversion rate compared with those in a traditional reactor versus reaction temperature for a permeate pressure of 0.2 bar.

To evaluate the system performance at a practical scene, the hourly DNI and corresponding Y_{H_2} were calculated using a permeate pressure of 0.2 bar with real separation energy and $\eta_{s\rightarrow e}$ of 15% for a typical sunny day in Beijing [50] during each of the four seasons (Figure 11). The change in Y_{H_2} is similar to that in DNI because the obtained energy amount decides the available heat for ESR reaction. As discussed above, reacting at higher temperatures (e.g., 300°C) results in high ESR conversions but does not coincide with the highest $\eta_{s\rightarrow f, \text{real}}$ due to the radiation loss. The variation in Y_{H_2} is similar to that in $\eta_{s\rightarrow f, \text{real}}$, and the highest Y_{H_2} occurs at 200°C . The highest Y_{H_2} of $22.4 \text{ mol}\cdot\text{m}^{-2}\cdot\text{h}^{-1}$ at noon occurs in June with the strongest radiation levels, whereas the highest Y_{H_2} during December is $16.6 \text{ mol}\cdot\text{m}^{-2}\cdot\text{h}^{-1}$ at noon. The total generation is also affected by the comparatively longer working hours in June versus the reduced working hours in December. Assuming that the annual amount of solar radiation is 2000 h [51,52], the annual Y_{H_2} , SCSR, and CDRR are estimated to be $72.6 \text{ kmol}\cdot\text{m}^{-2}\cdot\text{y}^{-1}$, $201.38 \text{ kg}\cdot\text{m}^{-2}\cdot\text{y}^{-1}$, and $493.40 \text{ kg}\cdot\text{m}^{-2}\cdot\text{y}^{-1}$, respectively. Notably, however, the temperature does not have a significant effect on the overall performance above 150°C .

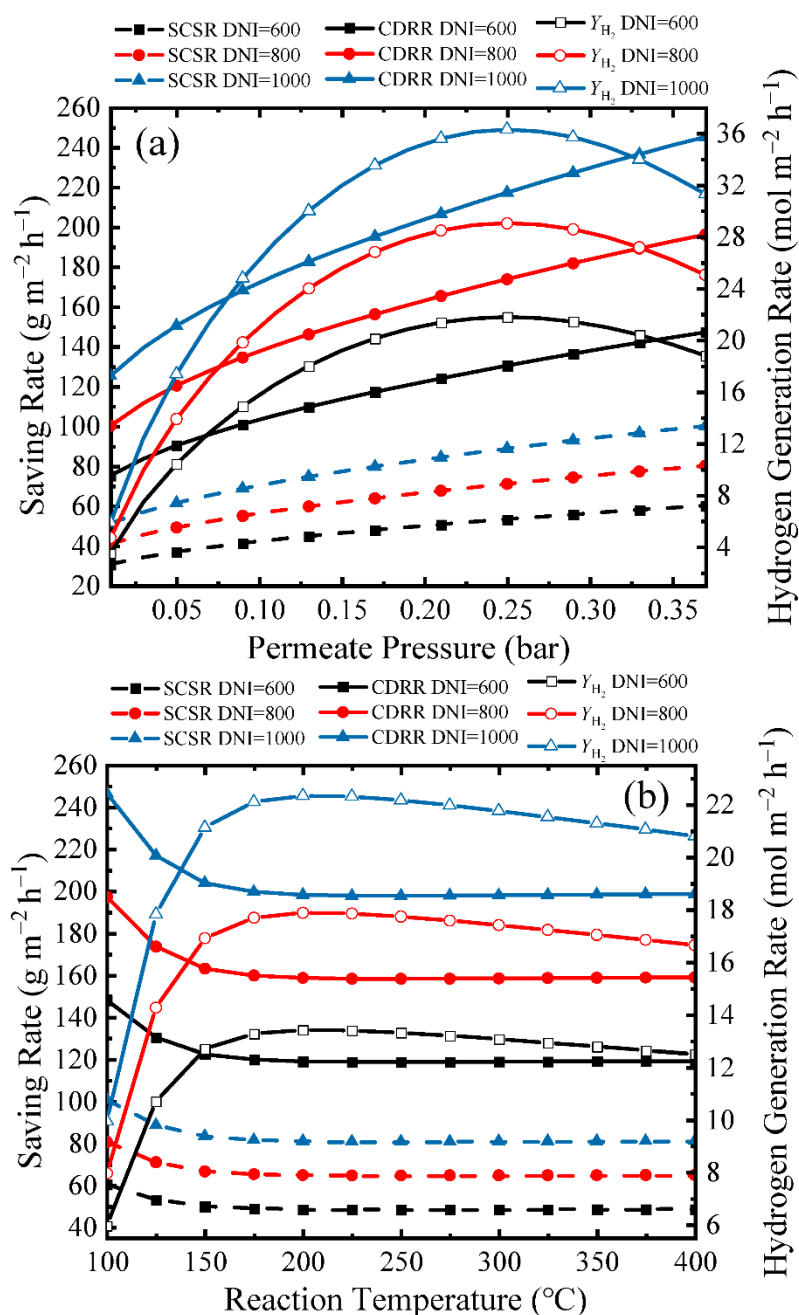


Figure 10. Variation of SCSR, CDRR, and Y_{H_2} with real separation energy and $\eta_{s\rightarrow e}$ of 15% versus (a) permeate pressure at a reaction temperature of 150 °C, (b) reaction temperature at a permeate pressure of 0.2 bar.

Compared with temperature, the permeate pressure has a more significant effect on the generated Y_{H_2} for each of the seasons. The results for generated Y_{H_2} are shown in Figure 12 for a reaction temperature of 150 °C with real separation energy and $\eta_{s\rightarrow e}$ of 15%. The optimum permeate pressure for Y_{H_2} is 0.25 bar, which produces a Y_{H_2} of 21.9 $mol\cdot m^{-2}\cdot h^{-1}$ at noon in June. The results shown in Figures 10 and 11 exhibit the promising application of the solar-driven ESR system under realistic operating conditions.

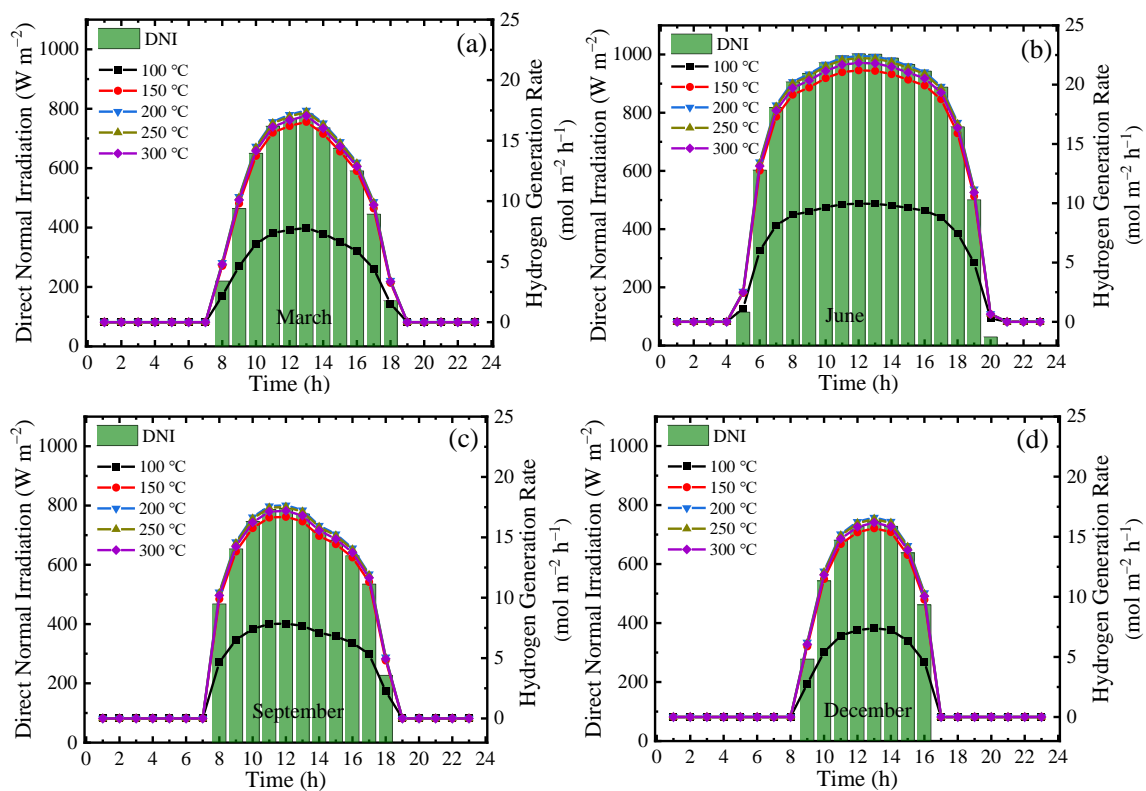


Figure 11. Variation in DNI and Y_{H_2} on a typical sunny day of different months for different reaction temperatures at a permeate pressure of 0.2 bar with real separation energy ($\eta_{s \rightarrow e} = 15\%$): (a) March; (b) June; (c) September; and (d) December.

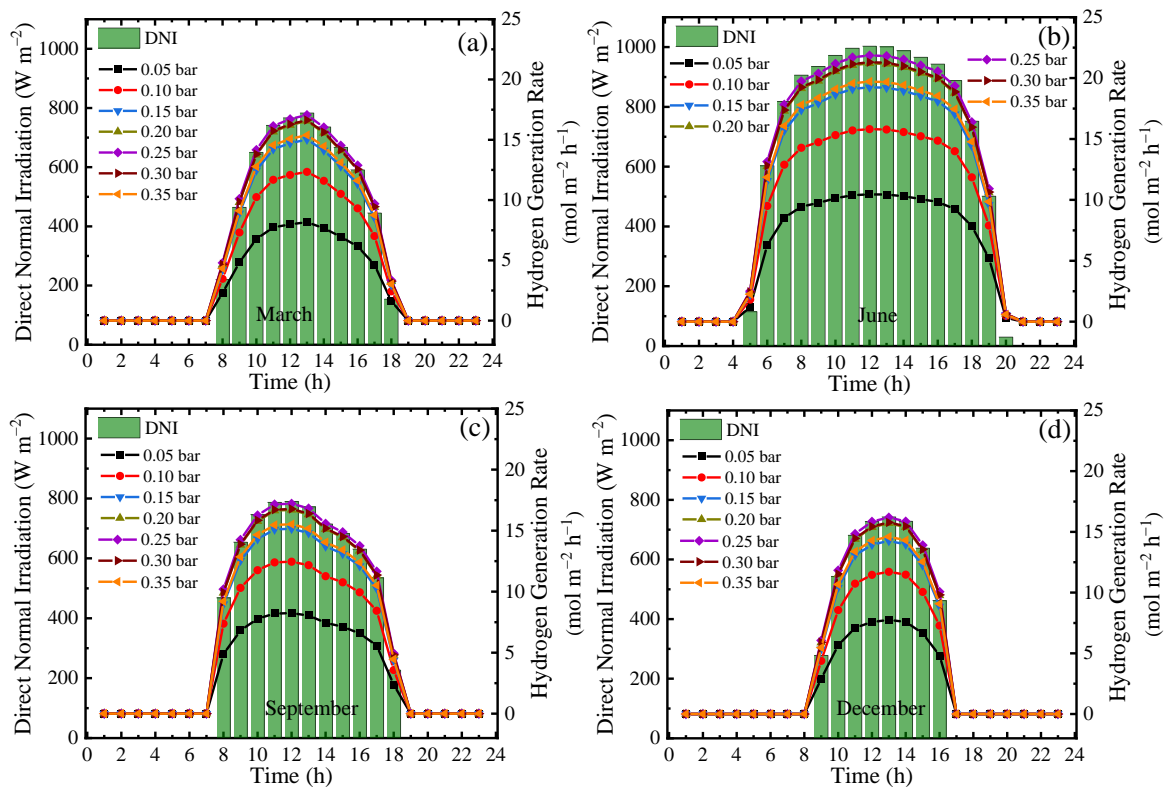


Figure 12. Variation in DNI and Y_{H_2} on a typical sunny day of different months for different permeate pressures at a reaction temperature of 150 °C with real separation energy ($\eta_{s \rightarrow e} = 15\%$): (a) March; (b) June; (c) September; and (d) December.

5. Conclusions

A novel solar-driven ESR system integrated with a membrane was proposed for solar energy storage and hydrogen production. This concept presents a promising approach for increasing conversion efficiency and has great potential for being utilized in distributed energy systems. The thermodynamic and environmental performances were analyzed, with the following highlighted conclusions:

- (1) An ESR system can improve the conversion rate at relatively low temperatures due to simultaneous separation of hydrogen. The theoretical conversion rate of the membrane reactor at 100 °C with permeate pressure of 0.01 bar is 98.3%, compared with only 14.8% for a traditional reactor configuration.
- (2) Solar energy can be utilized efficiently in this system. The first-law thermodynamic efficiency, solar-to-fuel efficiency, and exergy efficiency with separation exergy and $\eta_{s \rightarrow e}$ of 40% are 82.3%, 45.3%, and 70.4%, respectively, at 215 °C and 0.20 bar. Compared with a traditional reactor, the $\eta_{HHV,real}$ achieves the largest increment and can reach 12.0% at 130 °C with $\eta_{s \rightarrow e}$ of 40%.
- (3) In terms of the environmental performance of this solar-driven ESR system, higher efficiency leads to less fuel consumption and lower CO₂ emissions. The SCSR and CDRR can achieve maximums of 101 g·m⁻²·h⁻¹ and 247 g·m⁻²·h⁻¹ at 200 °C and 0.20 bar with a corresponding hydrogen generation rate of 22.4 mol·m⁻²·h⁻¹. The annual SCSR and CDRR are expected to be 201 kg·m⁻²·y⁻¹ and 493 kg·m⁻²·y⁻¹.

The proposed ESR membrane reactor provides insight into a means of efficient storage and conversion of solar energy, with potential for utilization in small energy systems, such as refueling stations for hydrogen fuel cell vehicles.

Author Contributions: Conceptualization, H.W.; methodology, H.W. and B.W.; software, B.W. and H.W.; validation, H.W., H.K., B.S. and J.W.; formal analysis, B.W. and S.-T.B.L.; investigation, H.W. and B.W.; resources, H.K., B.S. and J.W.; data curation, H.W. and B.W.; writing—original draft preparation, H.W. and B.W.; writing—review and editing, H.W., B.W., S.-T.B.L., H.K., B.S. and J.W.; visualization, B.W.; supervision, H.K., B.S. and J.W.; project administration, H.K., B.S. and J.W.; funding acquisition, H.W., H.K. and B.S. All authors have read and agreed to the published version of the manuscript.

Funding: This work was funded by the National Natural Science Foundation of China (No. 51906179, No. 52006124, and No. 52006089) and the China Scholarship Council (No. 201906275035). Jian WANG acknowledges the support of City University of Hong Kong through project 9610537.

Institutional Review Board Statement: Not applicable.

Informed Consent Statement: Not applicable.

Data Availability Statement: The data presented in this study are available on request from the corresponding author.

Conflicts of Interest: The authors declare no conflict of interest.

References

1. Kannan, N.; Vakeesan, D. Solar energy for future world—A review. *Renew. Sustain. Energy Rev.* **2016**, *62*, 1092–1105. [[CrossRef](#)]
2. Kong, H.; Hao, Y.; Wang, H. A solar thermochemical fuel production system integrated with fossil fuel heat recuperation. *Appl. Therm. Eng.* **2016**, *108*, 958–966. [[CrossRef](#)]
3. Kodama, T. High-temperature solar chemistry for converting solar heat to chemical fuels. *Prog. Energy Combust. Sci.* **2003**, *29*, 567–597. [[CrossRef](#)]
4. Hassanpouryouzband, A.; Joonaki, E.; Edlmann, K.; Haszeldine, R.S. Offshore Geological Storage of Hydrogen: Is This Our Best Option to Achieve Net-Zero? *ACS Energy Lett.* **2021**, *6*, 2181–2186. [[CrossRef](#)]
5. He, R.; Wang, Y.; Wang, H.; Lundin, S.-T.B.; Wang, B.; Kong, H.; Lu, X.; Wang, J.; Li, W. A mid/low-temperature solar-driven integrated membrane reactor for the dehydrogenation of propane—A thermodynamic assessment. *Appl. Therm. Eng.* **2021**, *193*, 116952. [[CrossRef](#)]
6. Wang, H.; Wang, B.; Kong, H.; Lu, X.; Hu, X. Thermodynamic Analysis of Methylcyclohexane Dehydrogenation and Solar Energy Storage via Solar-Driven Hydrogen Permeation Membrane Reactor. *Membranes* **2020**, *10*, 374. [[CrossRef](#)]

7. Zhao, Q.; Zhang, X.; Wang, H.; Liu, M.; Lundin, S.T.B.; Shu, S.; Konh, H.; Hu, X. Feasibility of solar thermochemical natural gas desul-phurization and hydrogen generation with a membrane reactor. *J. Clean. Prod.* **2021**, *312*, 127835. [[CrossRef](#)]
8. Sui, J.; Chen, Z.; Wang, C.; Wang, Y.; Liu, J.; Li, W. Efficient hydrogen production from solar energy and fossil fuel via water-electrolysis and methane-steam-reforming hybridization. *Appl. Energy* **2020**, *276*, 115409. [[CrossRef](#)]
9. Zhao, Q.; Su, B.; Wang, H.; He, A.; He, R.; Kong, H.; Hu, X. Mid/low-temperature solar hydrogen generation via dry reforming of methane enhanced in a membrane reactor. *Energy Convers. Manag.* **2021**, *240*, 114254. [[CrossRef](#)]
10. Hanaki, K.; Portugal-Pereira, J. The Effect of Biofuel Production on Greenhouse Gas Emission Reductions. *Biofuels Sustain.* **2018**, 53–71. [[CrossRef](#)]
11. Zhao, Y.; Damgaard, A.; Christensen, T. Bioethanol from corn stover—A review and technical assessment of alternative biotechnologies. *Prog. Energy Combust. Sci.* **2018**, *67*, 275–291. [[CrossRef](#)]
12. Chen, J.; Zhang, B.; Luo, L.; Zhang, F.; Yi, Y.; Shan, Y.; Liu, B.; Zhou, Y.; Wang, X.; Lü, X. A review on recycling techniques for bioethanol production from lignocellulosic biomass. *Renew. Sustain. Energy Rev.* **2021**, *149*, 111370. [[CrossRef](#)]
13. Costa, M.; Cerri, B.; Ceccato-Antonini, S.R. Ethanol addition enhances acid treatment to eliminate *Lactobacillus fermentum* from the fermentation process for fuel ethanol production. *Let. Appl. Microbiol.* **2018**, *66*, 77–85. [[CrossRef](#)]
14. Fang, Y.R.; Wu, Y.; Xie, G.H. Crop residue utilizations and potential for bioethanol production in China. *Renew. Sustain. Energy Rev.* **2019**, *113*, 109288. [[CrossRef](#)]
15. Ma, R.; Dominguez, B.C.; Dixon, A.G.; Ma, Y.H. CFD study of heat and mass transfer in ethanol steam reforming in a catalytic membrane reactor. *Int. J. Hydrogen Energy* **2018**, *43*, 7662–7674. [[CrossRef](#)]
16. Jia, H.; Xu, H.; Sheng, X.; Yang, X.; Shen, W.; Goldbach, A. High-temperature ethanol steam reforming in PdCu membrane reactor. *J. Membr. Sci.* **2020**, *605*, 118083. [[CrossRef](#)]
17. Lu, G.; da Costa, J.C.D.; Duke, M.; Giessler, S.; Socolow, R.; Williams, R.; Kreutz, T. Inorganic membranes for hydrogen production and purification: A critical review and perspective. *J. Colloid Interface Sci.* **2007**, *314*, 589–603. [[CrossRef](#)]
18. Dahlmeyer, J.; Garrison, T.; Garrison, T.; Darkey, S.; Massicotte, F.; Rebeiz, K.; Nesbit, S.; Craft, A. Effects of hydrogen exposure temperature on the tensile strength, microhardness and ductility of Pd/Ag (25wt.%) alloy. *Scr. Mater.* **2011**, *64*, 789–792. [[CrossRef](#)]
19. Pal, N.; Agarwal, M.; Maheshwari, K.; Solanki, Y.S. A review on types, fabrication and support material of hydrogen separation membrane. *Mater. Today Proc.* **2020**, *28*, 1386–1391. [[CrossRef](#)]
20. Yun, S.; Oyama, S.T. Correlations in palladium membranes for hydrogen separation: A review. *J. Membr. Sci.* **2011**, *375*, 28–45. [[CrossRef](#)]
21. Uemiya, S.; Matsuda, T.; Kikuchi, E. Hydrogen permeable palladium-silver alloy membrane supported on porous ceramics. *J. Membr. Sci.* **1991**, *56*, 315–325. [[CrossRef](#)]
22. Iulianelli, A.; Palma, V.; Bagnato, G.; Ruocco, C.; Huang, Y.; Veziroğlu, N.T.; Basile, A. From bioethanol exploitation to high grade hydrogen generation: Steam reforming promoted by a Co-Pt catalyst in a Pd-based membrane reactor. *Renew. Energy* **2018**, *119*, 834–843. [[CrossRef](#)]
23. Iulianelli, A.; Liguori, S.; Vita, A.S.; Italiano, C.; Fabiano, C.; Huang, Y.; Basile, A. The oncoming energy vector: Hydrogen produced in Pd-composite membrane reactor via bioethanol reforming over Ni/CeO₂ catalyst. *Catal. Today* **2016**, *259*, 368–375. [[CrossRef](#)]
24. Jin, Y.; Rui, Z.; Tian, Y.; Lin, Y.; Li, Y. Autothermal reforming of ethanol in dense oxygen permeation membrane reactor. *Catal. Today* **2015**, *264*, 214–220. [[CrossRef](#)]
25. Kong, H.; Kong, X.; Wang, H.; Wang, J. A strategy for optimizing efficiencies of solar thermochemical fuel production based on nonstoichiometric oxides. *Int. J. Hydrogen Energy* **2019**, *44*, 19585–19594. [[CrossRef](#)]
26. Li, W.; Wang, H.; Hao, Y. A PVTC system integrating photon-enhanced thermionic emission and methane reforming for efficient solar power generation. *Sci. Bull.* **2017**, *62*, 1380–1387. [[CrossRef](#)]
27. Wang, H.; Kong, H.; Pu, Z.; Li, Y.; Hu, X. Feasibility of high efficient solar hydrogen generation system integrating photovoltaic cell/ photon-enhanced thermionic emission and high-temperature electrolysis cell. *Energy Convers. Manag.* **2020**, *210*, 112699. [[CrossRef](#)]
28. Kalogirou, S. Solar thermal collectors and applications. *Prog. Energy Combust. Sci.* **2004**, *30*, 231–295. [[CrossRef](#)]
29. Sun, J.; Liu, Q.; Hong, H. Numerical study of parabolic-trough direct steam generation loop in recirculation mode: Characteristics, performance and general operation strategy. *Energy Convers. Manag.* **2015**, *96*, 287–302. [[CrossRef](#)]
30. Bai, Z.; Liu, Q.; Lei, J.; Jin, H. Investigation on the mid-temperature solar thermochemical power generation system with methanol decomposition. *Appl. Energy* **2018**, *217*, 56–65. [[CrossRef](#)]
31. Wang, H.; Wang, B.; Qi, X.; Wang, J.; Yang, R.; Li, D.; Hu, X. Innovative non-oxidative methane dehydroaromatization via solar membrane reactor. *Energy* **2020**, *216*, 119265. [[CrossRef](#)]
32. Tou, M.; Michalsky, R.; Steinfeld, A. Solar-Driven Thermochemical Splitting of CO₂ and In Situ Separation of CO and O₂ across a Ceria Redox Membrane Reactor. *Joule* **2017**, *1*, 146–154. [[CrossRef](#)]
33. Giaconia, A.; Iaquaniello, G.; Caputo, G.; Morico, B.; Salladini, A.; Turchetti, L.; Monteleone, G.; Giannini, A.; Palo, E. Experimental validation of a pilot membrane reactor for hydrogen production by solar steam reforming of methane at maximum 550 °C using molten salts as heat transfer fluid. *Int. J. Hydrogen Energy* **2020**, *45*, 33088–33101. [[CrossRef](#)]
34. Ogo, S.; Sekine, Y. Recent progress in ethanol steam reforming using non-noble transition metal catalysts: A review. *Fuel Process. Technol.* **2019**, *199*, 106238. [[CrossRef](#)]

35. Ma, R.; Dominguez, B.C.; Mardilovich, I.P.; Dixon, A.G.; Ma, Y.H. Experimental and simulation studies of the production of renewable hydrogen through ethanol steam reforming in a large-scale catalytic membrane reactor. *Chem. Eng. J.* **2016**, *303*, 302–313. [CrossRef]
36. Sousa, J.M.; Cruz, P.; Mendes, A. Modeling a catalytic polymeric non-porous membrane reactor. *J. Membr. Sci.* **2001**, *181*, 241–252. [CrossRef]
37. Catalano, J.; Baschetti, M.G.; Sarti, G.C. Hydrogen permeation in palladium-based membranes in the presence of carbon monoxide. *J. Membr. Sci.* **2010**, *362*, 221–233. [CrossRef]
38. Wang, H.; Hao, Y. Thermodynamic Study of Solar Thermochemical Methane Steam Reforming with Alternating H₂ and CO₂ Permeation Membranes Reactors. *Energy Procedia* **2017**, *105*, 1980–1985. [CrossRef]
39. Wang, H.; Hao, Y.; Kong, H. Thermodynamic study on solar thermochemical fuel production with oxygen permeation membrane reactors. *Int. J. Energy Res.* **2015**, *391*, 1790–1799. [CrossRef]
40. Roine, A. *HSC Chemistry*; Outokumpu Research Oy: Pori, Finland, 2002.
41. Wang, B.; Kong, H.; Wang, H.; Wang, Y.; Hu, X. Kinetic and thermodynamic analyses of mid/low-temperature ammonia decomposition in solar-driven hydrogen permeation membrane reactor. *Int. J. Hydrogen Energy* **2019**, *44*, 26874–26887. [CrossRef]
42. Wang, H.; Liu, M.; Kong, H.; Hao, Y. Thermodynamic analysis on mid/low temperature solar methane steam reforming with hydrogen permeation membrane reactors. *Appl. Therm. Eng.* **2019**, *152*, 925–936. [CrossRef]
43. Bulfin, B.; Call, F.; Lange, M.; Lübber, O.; Sattler, C.; Pitz-Paal, R.; Shvets, I.V. Thermodynamics of CeO₂ Thermochemical Fuel Production. *Energy Fuels* **2015**, *29*, 1001–1009. [CrossRef]
44. Jarrett, C.; Chueh, W.; Yuan, C.; Kawajiri, Y.; Sandhage, K.H.; Henry, A. Critical limitations on the efficiency of two-step thermochemical cycles. *Sol. Energy* **2016**, *123*, 57–73. [CrossRef]
45. Li, Y.; Zhang, N.; Cai, R. Low CO₂-emissions hybrid solar combined-cycle power system with methane membrane reforming. *Energy* **2013**, *58*, 36–44. [CrossRef]
46. Tu, H.; Liu, C. Calculation of CO₂ emission of standard coal. *Coal Qual Technol.* **2014**, *2*, 57–60.
47. Fletcher, E.A. Solar thermal processing: A review. *J. Solar Energy Eng.* **2001**, *123*, 63–74. [CrossRef]
48. Wang, H.; Li, W.; Liu, T.; Liu, X.; Hu, X. Thermodynamic analysis and optimization of photovoltaic/thermal hybrid hydrogen generation system based on complementary combination of photovoltaic cells and proton exchange membrane electrolyzer. *Energy Convers. Manag.* **2019**, *183*, 97–108. [CrossRef]
49. Sun, J.; Qiu, X.-P.; Wu, F.; Zhu, W.-T. H₂ from steam reforming of ethanol at low temperature over Ni/Y₂O₃, Ni/La₂O₃ and Ni/Al₂O₃ catalysts for fuel-cell application. *Int. J. Hydrogen Energy* **2005**, *30*, 437–445. [CrossRef]
50. System Advisor Model, Version 2016.3.14. Available online: <https://sam.nrel.gov/> (accessed on 27 November 2020).
51. Chen, Y.; Hu, W.; Sweeney, S. Resource availability for household biogas production in rural China. *Renew. Sustain. Energy Rev.* **2013**, *25*, 655–659. [CrossRef]
52. Hang, Q.; Jun, Z.; Xiao, Y.; Junkui, C. Prospect of concentrating solar power in China—The sustainable future. *Renew. Sustain. Energy Rev.* **2008**, *12*, 2505–2514. [CrossRef]